

DeepFRC: An End-to-End Deep Learning Model for Functional Registration and Classification

Siyuan Jiang¹, Yihan Hu¹, Wenjie Li¹, and Pengcheng Zeng^{1,*}

¹Institute of Mathematical Sciences, ShanghaiTech University, Shanghai, China

*Corresponding author: zengpch@shanghaitech.edu.cn

January 31, 2025

Equal Contribution: Siyuan Jiang, Yihan Hu and Pengcheng Zeng

Abstract

Functional data analysis (FDA) is essential for analyzing continuous, high-dimensional data, yet existing methods often decouple functional registration and classification, limiting their efficiency and performance. We present DeepFRC, an end-to-end deep learning framework that unifies these tasks within a single model. Our approach incorporates an alignment module that learns time warping functions via elastic function registration and a learnable basis representation module for dimensionality reduction on aligned data. This integration enhances both alignment accuracy and predictive performance. Theoretical analysis establishes that DeepFRC achieves low misalignment and generalization error, while simulations elucidate the progression of registration, reconstruction, and classification during training. Experiments on real-world datasets demonstrate that DeepFRC consistently outperforms state-of-the-art methods, particularly in addressing complex registration challenges. Code is available at: <https://github.com/Drivergo-93589/DeepFRC>.

Keywords: Functional Data Analysis; Deep Learning; Registration; Classification

1 Introduction

Functional data analysis (FDA) is a key area for analyzing data that varies continuously over domains like time, space, or other variables (Ramsay and Silverman, 2005; Ferraty and Vieu,

2006; Srivastava and Klassen, 2016). Functional data is ubiquitous in fields such as biomechanics, neuroscience, healthcare, and environmental science, appearing in datasets like growth curves, wearable device signals, EEGs, fMRI scans, and air pollution levels. Despite its wide applicability, FDA faces challenges stemming from the infinite-dimensional nature of functional data, as well as issues related to smoothness and misalignment, necessitating advanced analytical tools (Wang et al., 2016; Matuk et al., 2022).

1.1 Motivation

Two key tasks in FDA are functional registration (curve alignment) and classification. Registration aligns curves to remove phase variability, enabling meaningful comparisons (Srivastava et al., 2011), while classification assigns labels based on underlying curve features. Traditionally, these tasks are addressed separately, with pre-registration followed by classification. However, this decoupled approach is inefficient, as the label significantly influences the progression pace of the curves, and alignment can provide valuable insights for classification (Liu and Yang, 2009; Tang et al., 2022). Jointly analyzing curve alignment and classification accounts for both temporal and structural variations, offering a more comprehensive understanding of the data.

Deep learning has revolutionized data analysis across various domains by enabling automatic feature extraction, representation learning, and scalability (LeCun et al., 2015). In FDA, deep learning presents an opportunity to integrate registration and classification into a unified framework. However, its application remains underexplored, with existing studies primarily focused on improving either registration accuracy (Chen and Srivastava, 2021) or classification performance (Yao et al., 2021; Wang and Cao, 2024), but rarely addressing both simultaneously. To address this gap, we propose an end-to-end deep learning framework that combines functional data registration and classification, eliminating the need for separate preprocessing while leveraging neural networks to model the complex, non-linear relationships inherent in functional data.

1.2 Related Work

Functional registration is a critical step in FDA, aimed at aligning functional data to correct for phase variability (Ramsay and Silverman, 2005). Traditional approaches include landmark-based methods (Kneip and Gasser, 1992; Ramsay and Silverman, 2005), metric-based methods (Wang and Gasser, 1997; Ramsay and Li, 1998; Srivastava et al., 2011; Srivastava and Klassen, 2016), and model-based methods (Tang and Müller, 2008; Claeskens et al., 2010; Lu et al., 2017). While effective in some contexts, these methods face limitations such as high computational cost, manual intervention, and sensitivity to noise. Landmark-based methods, for example, require subjective and potentially impractical landmark selection (Marron et al., 2015). Recently, neural network-based

methods (Chen and Srivastava, 2021) have been proposed, but they are still typically used as preprocessing steps, disconnected from the downstream tasks.

Functional classification has traditionally relied on statistical methods like generalized functional regression (James, 2002; Müller, 2005) and functional principal component analysis (fPCA) (Hall et al., 2000; Leng and Müller, 2006), which involve dimension reduction followed by classification. However, these methods are limited by their reliance on handcrafted features and basis function selection, which restricts their adaptability to complex, non-linear data. The integration of deep learning into functional classification, as seen in works by Thind et al. (2020), Yao et al. (2021), and Wang and Cao (2024), addresses these issues, although they typically treat registration as a separate preprocessing task.

Few studies have integrated registration and classification within a unified framework for FDA. Lohit et al. (2019) proposed a Temporal Transformer Network (TTN) for time series classification, but it is not designed for functional data, neglecting the curve’s smoothness and infinite-dimensional nature, thus struggling with accurate alignment. More recently, Tang et al. (2022) introduced a two-level model for joint registration and classification, modeling warping functions via a mixed-effects approach. However, this model is heavily reliant on assumptions, computationally expensive, and not easily extendable to multi-class settings.

1.3 Contributions

In this work, we propose a novel deep learning model that seamlessly integrates functional registration and classification, expanding upon previous research. Our contributions are: (1) A method combining an alignment module for time-warping via elastic functional registration with a learnable basis representation for dimensionality reduction, enhancing both alignment and classification performance; (2) Two proofs demonstrating that our model achieves low misalignment error under the EFDA framework and low generalization error under mild regularity conditions; (3) Extensive experiments on simulated and real-world datasets, highlighting the model’s ability to jointly optimize registration and classification, superior performance over state-of-the-art methods, stability under basis expansion, and robustness to missing data. The paper follows the order of contributions outlined above.

2 The Model

Consider the data $\{(x_i(\mathbf{t}_i), y_i)\}_{i=1}^N$, where $x_i(\mathbf{t}_i) = (x_i(t_{i1}), \dots, x_i(t_{in}))^\top$ represents the observed values of functional data $x(t)$ at n time points for the i -th sample, and $y_i \in \{1, \dots, C\}$ denotes its class label. The functional data $x(t)$ is assumed to be a mean-square continuous process defined over $t \in [0, 1]$, and the observations are misaligned. We hypothesize the existence of an underlying

nonlinear time warping map $\gamma : t \mapsto \tilde{t}$ and a prediction function $f : x(\tilde{t}) \mapsto y$. Our goal is to estimate γ and f simultaneously by an end-to-end deep learning model. This allows us to align new functional data $x^*(\mathbf{t}^*)$ using $\gamma(\mathbf{t}^*)$ and classify it with $y^* = f(x^*(\gamma(\mathbf{t}^*)))$. In the following, we detail the development of our deep neural networks to approximate both mappings γ and f .

2.1 Neural Network Representation for Time Warping

Our approach firstly utilizes 1D convolutional neural networks (1D CNNs) to extract temporal features from functional data, capitalizing on their demonstrated effectiveness in capturing temporal patterns (Kiranyaz et al., 2016; Ince et al., 2016; Chen and Srivastava, 2021; Kiranyaz et al., 2021). These networks process observed functional data points to produce latent features, which are then used to construct time-warping functions, enabling better registration of functional data.

For an input sequence $X \in \mathbb{R}^{n \times k}$ (length n with k channels) and a kernel $W \in \mathbb{R}^{s \times k}$, the 1D convolution is defined as $\mathbf{z} = W \circledast X + \mathbf{b}$, where \circledast denotes the convolution operator. Using the rectified linear unit (ReLU) activation function $h(x) = \max\{0, x\}$, the latent features $\tau(\mathbf{x}_i) \in \mathbb{R}^{n \times 1}$ ($\mathbf{x}_i \triangleq x_i(\mathbf{t}_i)$) for the i -th sample are generated through a multi-layer 1D CNN module. The CNN architecture includes $l_1 - 1$ convolutional layers and a final fully connected layer, structured as:

$$\tau(\mathbf{x}_i) = h(W^{l_1}(\mathbf{h}(W^{l_1-1} \circledast \dots \mathbf{h}(W^1 \circledast \mathbf{x}_i + B^1) + \dots) + B^{l_1-1}) + \mathbf{b}^{l_1}), \quad (1)$$

where $\mathbf{h}(W^l \circledast X^{l-1} + B^l) \in \mathbb{R}^{k_l \times n_l}$ represents the matrix whose rows correspond to the ReLU-activated outputs (i.e. $h(\mathbf{z})$) of each kernel, and W^l and B^l are weight and bias terms of the l -th layer, respectively. The latent features $\tau(\mathbf{x}_i)$ encode the temporal structure of the observed data \mathbf{x}_i . These networks are parameterized by weights Θ_1 , with hyperparameters including the number of layers l_1 , kernel counts \mathbf{k} , and kernel sizes \mathbf{s} .

To construct a boundary-preserving diffeomorphic warping function, the latent features $\tau(\mathbf{x}_i)$ are transformed as:

$$\tilde{\gamma}_i(t_{ij}) = \frac{\sum_{\mu=0}^j \tau_{i\mu}^2}{\sum_{\nu=0}^n \tau_{i\nu}^2}, \quad j = 0, 1, \dots, n, \quad (2)$$

where $t_{i0} = 0$, $t_{in} = 1$, and $\tau_{i\mu}$ is the μ -th element of $\tau(\mathbf{x}_i)$. This ensures that $\tilde{\gamma}_i(0) = 0$, $\tilde{\gamma}_i(1) = 1$ and $\frac{d(\tilde{\gamma}_i(t))}{dt} > 0$, satisfying the requirements of a valid warping function (Chen and Srivastava, 2021). To reduce roughness and preserve the geometric structure, the warping function is further smoothed:

$$\gamma_i(t_{ij}) = \frac{\sum_{\mu=0}^j \tilde{\gamma}_{i\mu}}{\sum_{\nu=0}^n \tilde{\gamma}_{i\nu}}. \quad (3)$$

This smoothing step ensures a smooth and well-structured warping function (Chen and Srivastava, 2021).

2.2 Basis Representation for Aligned Function

By applying the time warping $\gamma_i(t_{ij})$ to the functional data \mathbf{x}_i , the aligned functional data $\tilde{x}_i(t)$ can be obtained using 1D linear interpolation on the points $\{(\gamma_i(t_{ij}), x_i(t_{ij}))\}_{j=1}^n$:

$$\tilde{x}_i(t) \triangleq \left[x(t_{ir}) + \frac{x_i(t_{i(r+1)}) - x_i(t_{ir})}{\gamma_i(t_{i(r+1)}) - \gamma_i(t_{ir})} (t - \gamma_i(t_{ir})) \right] \cdot \mathbb{1}_{\{\gamma_i(t_{ir}) \leq t \leq \gamma_i(t_{i(r+1)})\}}, \quad r = 0, 1, \dots, n, \quad (4)$$

where $\mathbb{1}_{\{\cdot\}}$ is the indicator function. This interpolation is both stable and computationally efficient (Berrut and Trefethen, 2004).

While traditional methods often discretize $\tilde{x}_i(t)$ into a high-dimensional vector $\tilde{\mathbf{x}}_i$ for input into neural networks, this approach suffers from the curse of dimensionality and fails to capture the smoothness of functional data, especially in noisy settings (Yao et al., 2021). To address these issues, we approximate $\tilde{x}_i(t)$ using basis expansion:

$$\tilde{x}_i(t) \approx \sum_{j=1}^K c_{ij} \phi_j(t), \quad (5)$$

where $\{\phi_j(t)\}_{j=1}^K$ are basis functions (e.g, Fourier, B-spline or polynomial basis) and $\{c_{ij}\}_{j=1}^K$ are coefficients to estimate. Using least squares, the coefficients $\mathbf{c}_i \triangleq (c_{i1}, \dots, c_{iK})$ are estimated as:

$$\tilde{\mathbf{c}}_i = \operatorname{argmin}_{\{c_{ij}\}} \int_0^1 \left[\tilde{x}_i(t) - \sum_{j=1}^K c_{ij} \phi_j(t) \right]^2 dx = G^{-1} \mathbf{d}_i, \quad (6)$$

where $G_{ij} = \int_0^1 \phi_i(t) \phi_j(t) dt$ and $d_{ij} = \int_0^1 \tilde{x}_i(t) \phi_j(t) dt$. These integrals can be computed using numerical methods like the composite Simpson’s rule (Süli and Mayers, 2003). Thus, the coefficients $\tilde{\mathbf{c}}_i$ are determined by $x_i(\mathbf{t}_i)$ and $\gamma_i(\mathbf{t}_i)$ through interpolation and basis projection, enabling efficient representation of the aligned functional data.

2.3 Neural Network-Based Functional Classifier

To predict the class label of the i -th sample, we design a fully connected feedforward neural networks with the input $\tilde{\mathbf{c}}_i (\in \mathbb{R}^K)$. The network consists of l_2 layers with n_l nodes on the l -th hidden layer ($l = l_1 + 1, \dots, l_1 + l_2 - 1$), and a softmax activation function $\sigma(x_j) = \frac{\exp(x_j)}{\sum_{i=1}^C \exp(x_i)}$ applied to the output layer:

$$\psi(\tilde{\mathbf{c}}_i) = \sigma(W^{l_1+l_2} (h(W^{l_1+l_2-1} \dots h(W^{l_1+1} \tilde{\mathbf{c}}_i + \mathbf{b}^{l_1+1}) + \dots) + \mathbf{b}^{l_1+l_2-1}) + \mathbf{b}^{l_1+l_2}), \quad (7)$$

where $W^l \in \mathbb{R}^{n_{l+1} \times n_l}$ and $\mathbf{b}^l \in \mathbb{R}^{n_{l+1}}$ are weight matrices and bias terms, respectively. The network output $\psi(\tilde{\mathbf{c}}_i) = (\psi_{i1}, \dots, \psi_{iC})^\top$ represents the probabilities of the observed functional data \mathbf{x}_i belonging to C classes. A new observed functional data $x^*(\mathbf{t}^*)$ is classified using $y^* = f(x^*(\gamma(\mathbf{t}^*))) = \operatorname{argmax}_j \psi_{ij}$. The parameters of this prediction module are denoted as Θ_2 . Key hyperparameters include the number of layers $l_2 (l_2 \geq 1)$ and the number of nodes \mathbf{n} .

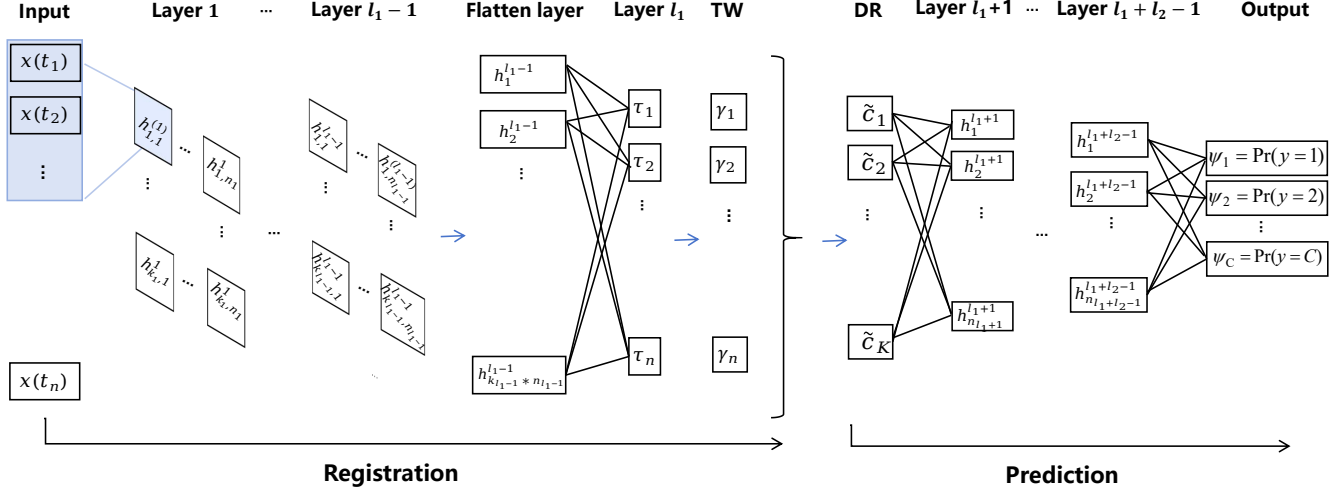


Figure 1: Overview of the model DeepFRC. This figure depicts the process of simultaneous registration and prediction for individual functional data $x(t)$. The light blue area highlights the 1D convolution operation, while the three blue arrows represent, from left to right, the flattening of the $(l_1 - 1)$ -th layer matrix, the warping operation, and the basis representation for the aligned function. Abbreviations: “TW” for Time Warping, and “DR” for Dimensionality Reduction.

2.4 Objective Function Formulation

We denote the overall parameters to estimate as $\Theta = \{\Theta_1, \Theta_2\}$. Given training data $\{(\mathbf{x}_i, y_i)\}_{i=1}^N$ (where $\mathbf{x}_i = x_i(\mathbf{t}_i), y_i \in \{1, \dots, C\}$), the objective function consists of two parts for estimating Θ .

Registration Loss: We adopt the elastic Riemannian metric square-root velocity function (SRVF) (Srivastava and Klassen, 2016) for registration, which overcomes limitations of the L^2 metric such as lack of invariance to warping, asymmetry, and the pinching effect (Marron et al., 2015; Srivastava and Klassen, 2016). The SRVF of $x(t)$ is defined as $q(t) = \text{sign}(\dot{x}(t))\sqrt{|\dot{x}(t)|}$, and for the warped function $x(\gamma(t))$, it becomes $(q \star \gamma)(t) \triangleq q(\gamma(t))\sqrt{\dot{\gamma}(t)}$ (Joshi et al., 2007; Srivastava and Klassen, 2016). For the i -th sample, we denote the observed SRVF as $Q_i(\gamma_i) = ((q_i \star \gamma_i)(t_{i1}), \dots, (q_i \star \gamma_i)(t_{in}))^\top$. Inspired by the work of Chen and Srivastava (2021), we define the registration loss as:

$$\mathcal{L}_1(\Theta_1) = \sum_{j=1}^C \frac{\sum_{i \in \{y_i=j\}} \|Q_i(\gamma_i) - \bar{Q}^{(j)}\|}{N^{(j)}} + \sum_{1 \leq u < v \leq C} \alpha_{uv} \|\bar{Q}^{(u)} - \bar{Q}^{(v)}\|^{-1}, \quad (8)$$

where $N^{(j)} = \#\{y_i = j\}, \bar{Q}^{(j)} = \frac{1}{N^{(j)}} \sum_{i \in \{y_i=j\}} Q_i(\gamma_i)$, $\|\cdot\|$ is Euclidean distance, and α_{uv} 's are hyperparameters. The first term aligns functions within each class by computing the elastic mean in SRVF space, while the second term encourages separation between class alignment centers. Larger α_{uv} for similar classes u and v improves class distinguishability by increasing the distance

between their alignment centers.

Classification Loss: The cross-entropy loss is given by

$$\mathcal{L}_2(\Theta) = -\frac{1}{N} \sum_{i=1}^N \sum_{j=1}^C y_{ij} \log \psi_{ij}, \quad (9)$$

where the label y_i is represented as a one-hot encoded vector $(y_{i1}, \dots, y_{iC})^\top$ where all elements are set to zero except for the element that corresponds to the active class, which is set to one.

The combined objective is:

$$\mathcal{L}(\Theta) = \mathcal{L}_1(\Theta_1) + \alpha_2 \mathcal{L}_2(\Theta) + \frac{1}{2} \alpha_3 \|\Theta\|_F^2, \quad (10)$$

where α_2 balances registration and classification, and the Frobenius norm $\|\Theta\|_F^2$ serves as L_2 -regularization to enhance generalization. Minimizing \mathcal{L}_1 aligns functions across classes while aiding classification, especially for similar classes, while minimizing \mathcal{L}_2 predicts class labels and improves alignment by enhancing class separation.

Integrating Subsections 2.1-2.4, we propose an end-to-end deep learning model, termed DeepFRC, for functional data registration and prediction (Figure 1).

2.5 Algorithm and Model Selection

The objective function (Eq. (10)) is optimized using stochastic gradient descent to estimate the network parameters in Θ . We employ the AdamW optimizer (Ilya and Frank, 2019), which is computationally efficient and particularly effective for models with a large number of parameters (Diederik and Lei, 2015). Gradients of the objective function with respect to each parameter $\theta \in \Theta$ are derived using the chain rule, as shown in Eqs. (A.1) and (A.2) of Appendix A. The full training procedure is detailed in Algorithm 1.

To improve efficiency, robustness, and interpretability, we integrate modern techniques into the 1D CNN module (Eq. (1)), including max pooling (Nagi et al., 2011), 1D batch normalization (Ioffe and Szegedy, 2015), and global averaging (Krizhevsky et al., 2012). Fourier expansion is employed for the basis representation of aligned functions. Network structure-related hyperparameters can be determined using data-splitting methods (Wang et al., 2023). A fixed hyperparameter configuration: $l_1 = 4$, $\mathbf{k} = (16, 32, 64)$, $\mathbf{s} = (3, 3, 3)$, $K = 100$, $l_2 = 2$, and $\mathbf{n} = (8, 4)$, consistently performs well across both simulated dataset (Section 4.1) and real-world datasets (Section 4.2). More details on model selection are provided in Appendix B.

3 Theoretical Analysis

We now discuss the theoretical properties of the proposed model, demonstrating that it achieves low misalignment error under EFDA framework and low generalization error under mild regularity

Algorithm 1 Training DeepFRC

Require: Training data $\{(x_i(\mathbf{t}_i), y_i)\}_{i=1}^N$

- 1: **Set Hyperparameters:** Network structure $\{l_1, \mathbf{k}, \mathbf{s}, l_2, \mathbf{n}, K\}$, loss-related $\{\alpha_{uv}, \alpha_2, \alpha_3\}$, and training parameters $\boldsymbol{\eta}$ (epochs E , batch size, learning rate, etc.)
 - 2: **Initialize Parameters** $\Theta = \Theta_{\text{initial}}$
 - 3: **for** $e = 1$ to E **do**
 - 4: **Forward Propagation:**
 - (1) Compute $\gamma_i(t)$ for each $x_i(\mathbf{t}_i)$
 - (2) Warp $x_i(\mathbf{t}_i)$ to obtain $\tilde{\mathbf{x}}_i$, calculate its SRVF $Q_i(\gamma_i)$, and extract coefficients $\tilde{\mathbf{c}}_i$
 - (3) Pass $\tilde{\mathbf{c}}_i$ through the classifier to compute $\psi(\tilde{\mathbf{c}}_i)$
 - (4) Compute the loss $\mathcal{L}(\Theta)$
 - 5: **Backward Propagation:** Update Θ via AdamW optimizer using $\frac{\partial \mathcal{L}(\Theta)}{\partial \theta}, \theta \in \Theta$
 - 6: **end for**
 - 7: **Return** Trained DeepFRC with optimized parameters Θ^*
-

conditions. Detailed proofs are provided in Appendices C and D.

The phase variability is modeled using monotone and smooth transformations within the set $\Gamma = \{\gamma : [0, 1] \rightarrow [0, 1] \mid \gamma(0) = 0, \gamma(1) = 1, \dot{\gamma} > 0\}$. Under the framework of elastic functional data analysis (EFDA) (Srivastava et al., 2011), the optimal warpings are defined as:

$$\gamma^* = \underset{\{\gamma_i\}}{\operatorname{argmin}} Q_{\text{reg}}(\gamma) \triangleq \underset{\{\gamma_i\}}{\operatorname{argmin}} \sum_{j=1}^C \frac{\sum_{i \in \{y_i=j\}} \|Q_i(\gamma_i) - \bar{Q}^{(j)}\|}{N^{(j)}}, \gamma_i \in \Gamma, \text{ where "reg" means "registration".}$$

For any other estimated warping $\hat{\gamma}$, the misalignment error can be quantified as

$$\Delta Q_{\text{reg}}(\gamma^*, \hat{\gamma}) \triangleq |Q_{\text{reg}}(\gamma^*) - Q_{\text{reg}}(\hat{\gamma})|.$$

Theorem 3.1 (Low Misalignment Error). *Assume that: (i) The proposed deep neural network has sufficient capacity, and (ii) $\gamma(t) \in \Gamma \cap \mathbf{C}^1$ and $q(t)$ (the SRVF of $x(t)$) is continuous and bounded for any individual curve $x(t)$.*

Then, for any $\epsilon > 0$, there exists an estimated $\hat{\gamma}$ generated by the proposed model such that:

$$\Delta Q_{\text{reg}}(\gamma^*, \hat{\gamma}) < \epsilon.$$

Remark 3.2. While Theorem 3.1 guarantees low registration error in theory, verifying this practically is challenging since the true warpings γ^* are not easily obtainable. This is due to the difficulty of achieving global optimization for $\min(Q_{\text{reg}}(\gamma))$. However, the validity of the result can be assessed through simulation studies, where true warpings are provided.

We further show that the proposed model achieves a small generalization error. Let $\hat{f}_{\Theta} : \mathbf{x} \rightarrow y$ represent the mapping of the proposed DeepFRC model with a fixed architecture. Define the

population risk and empirical risk as $R(\Theta) = \mathbb{E}[l(\hat{f}_\Theta(\mathbf{x}), y)]$ and $R_n(\Theta) = \frac{1}{N} \sum_{i=1}^N l(\hat{f}_\Theta(\mathbf{x}_i), y_i)$, respectively, where l denotes the individual loss function. The generalization error is given by

$$\Delta R_{\text{gen}}(\hat{\Theta}) = |\mathbb{E}_{S,A}[R(\hat{\Theta}) - R_n(\hat{\Theta})]|,$$

where $\hat{\Theta}$ is the parameter set estimated via a random algorithm A based on a random sample S . During training, we assume the AdamW optimizer uses an inverse time decay or a custom decay function to ensure the learning rate α_t is monotonically non-increasing with $\alpha_t \leq c_0/t$, for some constant $c_0 > 0$, and that the algorithm runs for T_0 steps. The following result builds upon Theorem 3.8 from Hardt et al. (2016) and Theorem 2 from Yao et al. (2021).

Theorem 3.3 (Low Generalization Error). *Assume that: (i) There exists $\epsilon_0 > 0$, such that $|\bar{Q}^{(u)} - \bar{Q}^{(v)}| \geq \epsilon_0$ for $1 \leq u < v \leq C$ and $\psi_{ij} \geq \epsilon_0$, and (ii) The weight Θ is restricted to a compact region.*

Then, for the weights $\hat{\Theta}$ estimated by the proposed model, there exists a constant $c_0 > 0$, such that

$$\Delta R_{\text{gen}}(\hat{\Theta}) \lesssim \frac{T_0^{1-1/c_0}}{N}.$$

Remark 3.4. Assumption (i) in Theorem 3.3 is reasonable and easily satisfied. First, each class should exhibit a unique alignment pattern, meaning the corresponding \bar{Q} values are distinct across classes. Second, by modifying the softmax function in the last layer of DeepFRC as: $\sigma(x_j) = \frac{\exp(x_j) + \beta}{\sum_{i=1}^C (\exp(x_i) + \beta)}$, it is possible to select a constant β such that each probability ψ_{ij} is at least ϵ_0 .

4 Experiments

We present the results of functional data registration and classification using DeepFRC, evaluated on both simulated and real-world datasets. Simulated data provides insights into registration, reconstruction, and classification progression during training. Real-world datasets allow for performance comparisons with classical methods. To test model generalization, training sets are deliberately smaller than test sets.

Evaluation Metrics: We evaluate registration performance using the metric $\Delta Q_{\text{reg}}(\gamma^*, \hat{\gamma})$ within the EFDA framework. This metric is applicable only to simulated datasets, as they provide true warping functions γ^* or underlying true curves. Another metric for alignment assessment is the total variance (TV) under the \mathbb{L}_2 norm (Chen and Srivastava, 2021):

$$\text{TV} = \frac{1}{N} \sum_{j=1}^C \sum_{i \in \{y_i=j\}} \|x_i \circ \gamma_i - \frac{1}{N^{(j)}} \sum_{i \in \{y_i=j\}} x_i \circ \gamma_i\|.$$

We propose an adjusted total variance (ATV) defined as:

$$\text{ATV} = \frac{1}{\binom{C}{2}} \sum_{1 \leq u < v \leq C} \frac{\text{TV}_{uv}}{d(\text{mean}(\tilde{x}_u), \text{mean}(\tilde{x}_v))},$$

where TV_{uv} is the total variation between classes u and v , and $\text{mean}(\tilde{x})$ denotes the mean function of the aligned curve \tilde{x} . ATV accounts for the distance between class mean functions, making it more suitable for alignment evaluation of similar classes. Both TV and ATV are applicable to simulated and real-world datasets. Lower values of ΔQ_{reg} , TV, and ATV indicate better alignment.

To assess DeepFRC’s ability to recover the underlying smooth process of aligned functional data, we compute the Pearson’s correlation coefficient $\rho(\mathbf{c}^*, \hat{\mathbf{c}})$ between the true and estimated Fourier basis coefficients. This metric is used only in simulations, as \mathbf{c}^* can only be computed when the true curves are known. Higher values of ρ indicate better reconstruction.

For classification performance, we evaluate accuracy (ACC) and F_1 -score, with the latter providing a more balanced measure of performance. The classification accuracy is defined as:

$$\text{ACC} = \frac{1}{N} \sum_{i=1}^N \mathbb{1}_{\{\hat{y}_i = y_i\}},$$

where \hat{y}_i and y_i are the predicted and true class labels, respectively. The F_1 -score is calculated as:

$$F_1\text{-score} = \frac{2 \times \text{Precision} \times \text{Recall}}{\text{Precision} + \text{Recall}}.$$

We use the macro-averaged F_1 -score (Sokolova and Lapalme, 2009) for multi-class classification. Higher values of ACC and F_1 -score indicate better classification performance.

4.1 Simulation

Data Generation: We first generate a balanced two-class functional dataset $\{x_i(t), y_i\}_{i=1}^n$, where the functional data $x(t)$ is composed of amplitude and phase functions for $t \in [0, 1]$. The amplitude function is defined as the sum of two Gaussian functions: $z_i(t|a_i, \mu, \sigma_i) = a_i \cdot \exp\left(-\frac{1}{2} \frac{(t-\mu)^2}{\sigma_i^2}\right)$, where a_i and σ_i are random variables uniformly distributed, and μ is a fixed constant. The phase function

$\gamma_i(t)$ is defined as: $\gamma_i(t) = \begin{cases} \frac{\exp(b_i t) - 1}{\exp(b_i) - 1}, & \text{if } b_i \neq 0, \\ t, & \text{otherwise,} \end{cases}$ where $b_i \sim U(-1.5, 1.5)$. These functions are

commonly used to model functional data with phase variation Kneip and Ramsay (2008); Tucker et al. (2013). We then generate the simulated dataset as follows:

$$x_i(t) = \begin{cases} \sum_{j=1}^2 z_i(\gamma_i(t)|a_i^{(0j)}, \mu^{(0j)}, \sigma_i^{(0j)}), & \text{if } y_i = 0, \\ \sum_{j=1}^2 z_i(\gamma_i(t)|a_i^{(1j)}, \mu^{(1j)}, \sigma_i^{(1j)}), & \text{if } y_i = 1, \end{cases}$$

where the parameters $\{a_i^{(cj)}, \mu^{(cj)}, \sigma_i^{(cj)}\}_{j=1}^2$, $c = 0, 1$, are detailed in Table A1 of Appendix E.1. A sample size of $n = 6000$ is chosen, with each functional curve consisting of 1000 time points.

Results: Figure 2 illustrates the effect of iterative optimization in DeepFRC on the simulated dataset. Figure 2(a) shows the raw curves of two classes (yellow and blue) with registration issues, which are challenging to distinguish visually. As shown in Figures 2(a)-(d), alignment improves progressively with the number of epochs, evidenced by the curves becoming more centered for each class, making them easier to differentiate. This process visually shows the mutual benefit of alignment and classification. Figure 2(e) demonstrates that the Pearson correlation coefficient $\rho(\mathbf{c}^*, \hat{\mathbf{c}})$ increases rapidly over epochs, reaching nearly 1 by epoch 50, indicating DeepFRC’s strong reconstruction capability for the true unwarped functional data. Figures 2(f)-(g) show the progression of alignment, assessed by $\Delta Q_{\text{reg}}(\gamma^*, \hat{\gamma})$, TV and ATV, and classification performance, evaluated by ACC and F_1 -score, all improving steadily with increasing epochs. Finally, Figure 2(h) presents the total loss function progression, which includes the registration loss (Eq. (8)) and classification loss (Eq. (9)). All three loss components decrease sharply before epoch 50 and stabilize near zero thereafter. Visualization of alignment on the simulated test set is provided in Figure A1 of Appendix E.1, with evaluation metrics showing $\rho = 0.976$, $\Delta Q_{\text{reg}} = 0.056$, TV = 3.611, ATV=0.504, ACC = 1.000 and F_1 -score = 1.000, demonstrating excellent generalization performance.

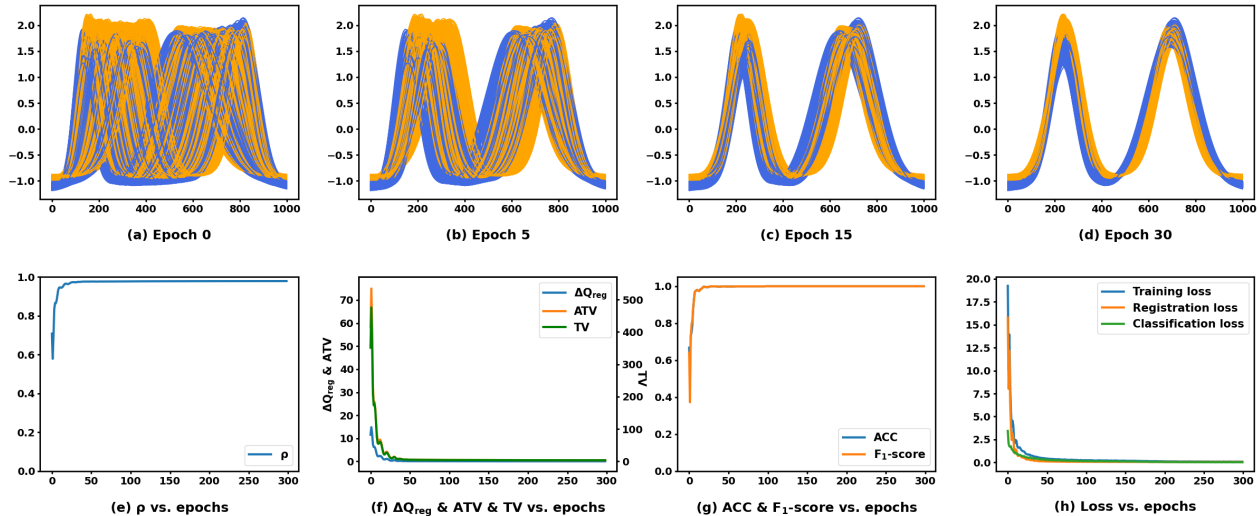


Figure 2: Contribution of iterative optimization in training DeepFRC on simulated two-class (yellow and blue) data. (a)-(d) depict the progression of registration at Epochs 0, 5, 15, and 30. (e)-(h) show the improvement in reconstruction (ρ), registration (ΔQ_{reg} , TV and ATV), classification (ACC and F_1 -score), and loss over SGD epochs.

4.2 Real Data Application

Real Data: Time series data is often treated as functional data in Functional Data Analysis (FDA) (Ramsay and Silverman, 2002, 2005). To evaluate DeepFRC, we select four time series datasets from the UCR Time Series Classification Archive (www.timeseriesclassification.com), each exhibiting registration challenges. The datasets are compared with baseline models: (a) **Wave:** The Wave dataset consists of eight simple gestures captured using accelerometers in the X, Y, and Z dimensions across 8 classes. For this experiment, we use the X dimension of classes 2 and 8, with 1120 curves and 315 time points per curve. (b) **Yoga:** The Yoga dataset includes two actors performing yoga poses in front of a green screen. Each pose is converted into a one-dimensional time series by outlining and measuring the distance to the center. The dataset contains 3300 samples with 426 time points each. (c) **Symbol:** The Symbol dataset includes data from 13 participants replicating random symbols, with 3 symbols and 6 classes. We use two subsets with misalignment: one with two classes (343 curves) and one with three classes (510 curves). The Wave and Symbol datasets are balanced, while Yoga is not. More details on the real-world datasets are provided in Appendix E.2

Baseline Models: We compare DeepFRC with six classic baseline models, using TV, ATV, ACC, and F_1 -score to assess alignment and classification performance. The models are: (1) TTN (Lohit et al., 2019): A method for joint alignment and classification of discrete time series but does not account for curve smoothness. (2) SrvfRegNet (Chen and Srivastava, 2021): An unsupervised method that aligns raw functional data via a 1D CNN. (3) FCNN_{raw}: A model that discretizes raw functional data into a vector, inputting it into a fully connected neural network. (4) FCNN_{fourier}: A model that transforms the functional data into Fourier basis coefficients and then feeds the resulting vector into a fully connected neural network. (5) FuncNN (Thind et al., 2020): A model that inputs entire functional curves directly into a fully connected neural network. (6) ADAFNN (Yao et al., 2021): A model that inputs entire functional curves, adapting the bases during learning. We evaluate registration performance for model (2) and classification performance for models (3)-(6), as model (2) does not support classification, and models (3)-(6) do not support registration. To ensure a fair comparison, the network architecture of SrvfRegNet is set to match the 1D CNN module of DeepFRC, while the architectures of FCNN_{raw} and FCNN_{fourier} are set to match the prediction module of DeepFRC (the input dimension adjusted as n for FCNN_{raw}).

Results: Implementation details of these models for the real data are provided in Appendix E.3. All baseline models are trained until their best performance is achieved. Table 1 compares alignment and classification performance across datasets. DeepFRC and TTN are the only methods capable of both aligning and classifying curves. Unlike TTN, DeepFRC employs EFDA for alignment, fully exploiting the smoothness of the curves, leading to superior alignment and classification performance. DeepFRC outperforms TTN on the Wave and Symbol (two cases) datasets in

both alignment and classification. On the Yoga dataset, DeepFRC achieves similar ACC and F_1 -score as TTN but surpasses it in alignment. Figure 3 shows that DeepFRC provides more reasonable alignment than TTN on the Symbol dataset with three classes (blue, yellow, purple), where TTN distorts the yellow and purple curves. Compared with SrvfRegNet, which does not use label information, DeepFRC performs better in alignment across all datasets, as measured by ATV. SrvfRegNet’s low TV values on Symbol datasets result from pushing similar classes too close, making them hard to distinguish (see yellow and blue curves in Figure 3(d)). Additional visualizations comparing registration performance among DeepFRC, TTN, and SrvfRegNet are available in Figure A2 of Appendix E.3. Compared to models like FCNN_{raw}, FCNN_{fourier}, FuncNN, and ADAFNN, which lack functional registration, DeepFRC consistently outperforms them in classification across all datasets, achieving a higher F_1 -score (but lower ACC) on the imbalanced Yoga dataset. This highlights the benefit of alignment in improving classification performance. Finally, Figure A3 of Appendix E.3 shows the training loss versus epochs for DeepFRC across all four datasets, highlighting the algorithm’s convergence.

Table 1: Comparison of registration and classification results between DeepFRC and six baseline models across four real datasets. Bold numbers indicate the best results.

MODELS	Wave				Yoga				Symbol(2 classes)				Symbol(3 classes)			
	Registration		Classification		Registration		Classification		Registration		Classification		Registration		Classification	
	TV	ATV	ACC	F_1 -score	TV	ATV	ACC	F_1 -score	TV	ATV	ACC	F_1 -score	TV	ATV	ACC	F_1 -score
DeepFRC	113	5.6	96.4%	0.965	239	16.2	89.8%	0.909	110	4.8	96.0%	0.959	74	3.2	96.3%	0.963
TTN	158	6.3	94.7%	0.948	318	57.7	89.4%	0.904	187	8.6	92.0%	0.918	134	4.5	93.3%	0.933
SrvfRegNet	138	7.3	-	-	245	136.0	-	-	93	14.1	-	-	59	6.5	-	-
FCNN _{raw}	-	-	95.7%	0.958	-	-	81.8%	0.832	-	-	90.0%	0.893	-	-	92.0%	0.920
FCNN _{fourier}	-	-	94.4%	0.946	-	-	83.1%	0.846	-	-	91.0%	0.905	-	-	94.7%	0.947
FuncNN	-	-	95.1%	0.933	-	-	91.6%	0.907	-	-	91.8%	0.899	-	-	94.7%	0.947
ADAFNN	-	-	94.4%	0.946	-	-	75.9%	0.775	-	-	92.0%	0.920	-	-	95.7%	0.957

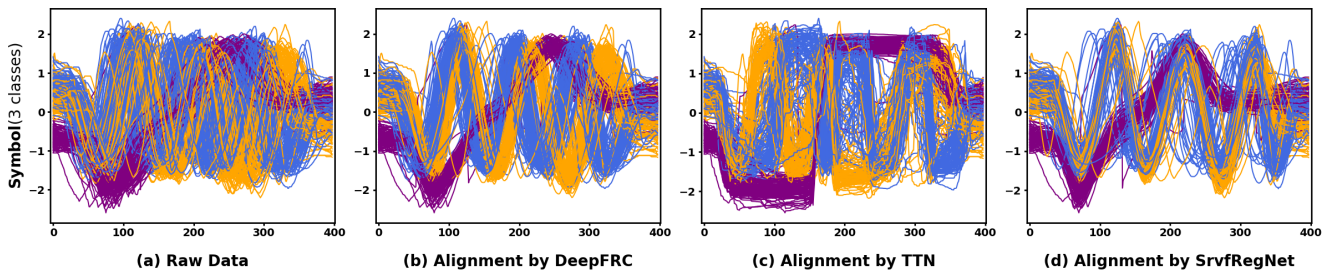


Figure 3: Comparison of alignment performance by DeepFRC, TTN and SrvfRegNet on the Symbol dataset with three classes (blue, yellow and purple).

5 Discussion

Stability with Respect to Basis Expansion: The basis functions $\{\phi_j(t)\}_{j=1}^K$ in Eq. (5) can be selected from Fourier, B-spline, or polynomial bases. Figure 4 compares the registration and classification performance of DeepFRC using these three basis expansions across all real-world datasets in Section 4.2, while keeping the model architecture and hyperparameters constant. The results indicate similar performance across all three basis types, demonstrating that DeepFRC is stable with respect to the choice of basis expansion. This suggests that, within the end-to-end deep learning framework, the selection of basis expansion has a minimal impact on both registration and classification performance. Further details on the B-spline and polynomial bases are provided in Appendix E.3.

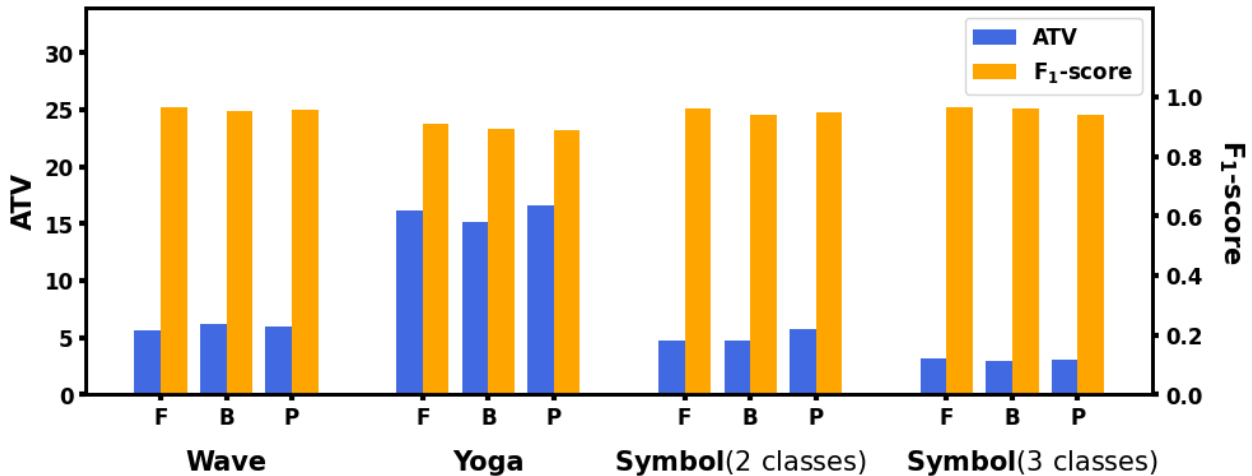


Figure 4: Performance of DeepFRC with different basis expansions across all real data in Section 4.2. “F”: Fourier; “B”: B-spline; “P”: Polynomial.

Robustness to Missing Data: To evaluate DeepFRC’s robustness to missing data, we tested the model with varying levels of missing observations. For each real-world dataset in Section 4.2, we randomly selected half of the samples and removed 5% and 10% of the observations from these selected samples, respectively. The missing values were then estimated using interpolation or extrapolation with Fourier splines (Wahba, 1990). The preprocessed data was then fed into DeepFRC using the same model architecture and hyperparameter settings as for the complete data. As shown in Figure 5, the registration and classification performance with 5% and 10% missing data closely resemble that of the complete data. The only exception is the Yoga dataset, where the alignment performance slightly decreases with higher missing rates due to increased noise and potential errors in the smoothing process. Overall, these results demonstrate that DeepFRC is robust to small amounts of missing data when appropriate smoothing techniques are applied.

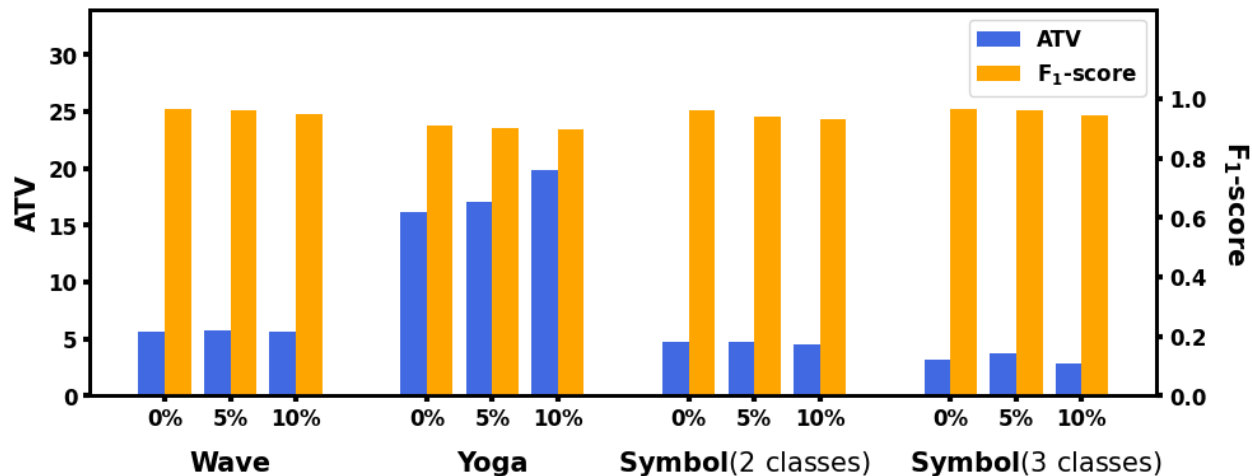


Figure 5: Performance of DeepFRC with different missing rates for raw data across four real-world datasets.

6 Conclusion

This work introduces a robust framework for joint functional registration and classification, backed by theoretical guarantees and extensive empirical validation. Our method not only outperforms state-of-the-art techniques but also provides a stable and reliable solution for real-world data scenarios, even with missing information.

References

- Berrut, J. P. and Trefethen, L. (2004). Barycentric lagrange interpolation. *SIAM Review*, 40(3):501–517.
- Chen, C. and Srivastava, A. (2021). Srvfregnet: Elastic function registration using deep neural networks. In *2021 IEEE/CVF Conference on Computer Vision and Pattern Recognition Workshops (CVPRW)*, pages 4457–4466.
- Claeskens, G., Silverman, B. W., and Slaets, L. (2010). A multiresolution approach to time warping achieved by a bayesian prior-posterior transfer fitting strategy. *Journal of the Royal Statistical Society: Series B*, 72(5):673–694.
- Cybenko, G. (1989). Approximation by superpositions of a sigmoidal function. *Mathematics of Control, Signals and Systems*, 2(4):303–314.
- Diederik, P. K. and Lei, B. (2015). Adam: a method for stochastic optimization. *International Conference on Learning Representations*.

- Ferraty, F. and Vieu, P. (2006). *Nonparametric Functional Data Analysis: Theory and Practice*. Springer Science & Business Media.
- Funahashi, K.-I. (1989). On the approximate realization of continuous mappings by neural networks. *Neural Networks*, 2(3):183–192.
- Hall, P., Poskitt, D. S., and Presnell, B. (2000). A functional data analytic approach to signal discrimination. *Technometrics*, 43:1–9.
- Hardt, M., Recht, B., and Singer, Y. (2016). Train faster, generalize better: Stability of stochastic gradient descent. *Proceedings of the 33rd International Conference on Machine Learning*, 48:1225–1234.
- Hornik, K. (1991). Approximation capabilities of multilayer feedforward networks. *Neural Networks*, 4(2):251–257.
- Ilya, L. and Frank, H. (2019). Decoded weight decay regularization. *International Conference on Learning Representations*.
- Ince, T., Kiranyaz, S., Eren, L., Askar, M., and Gabbouj, M. (2016). Real-time motor fault detection by 1-d convolutional neural networks. *IEEE Transactions on Industrial Electronics*, 63(11):7067–7075.
- Ioffe, S. and Szegedy, C. (2015). Batch normalization: Accelerating deep network training by reducing internal covariate shift. *International Conference on Machine Learning*, pages 448–456.
- James, G. M. (2002). Generalized linear models with functional predictors. *Journal of the Royal Statistical Society: Series B*, 64:411–432.
- Joshi, S., Klassen, E., Srivastava, A., and Jermyn, I. (2007). A novel representation for riemannian analysis of elastic curves in rn. In *2007 IEEE Conference on Computer Vision and Pattern Recognition*, pages 1–7.
- Kiranyaz, S., Avci, O., Abdeljaber, O., Ince, T., Gabbouj, M., and Inman, D. J. (2021). 1d convolutional neural networks and applications: A survey. *Mechanical Systems and Signal Processing*, 151:107398.
- Kiranyaz, S., Ince, T., and Gabbouj, M. (2016). Real-time patient-specific eeg classification by 1-d convolutional neural networks. *IEEE Trans. Biomed. Eng.*, 63(3):664–675.
- Kneip, A. and Gasser, T. (1992). Statistical tools to analyze data representing a sample of curves. *Annals of Statistics*, 20(3):1266–1305.

- Kneip, A. and Ramsay, J. O. (2008). Combining registration and fitting for functional models. *Journal of the American Statistical Association*, 103(483):1155–1165.
- Krizhevsky, A., Sutskever, I., and Hinton, G. E. (2012). Imagenet classification with deep convolutional neural networks. *Advances in neural information processing systems*, (25):1097–1105.
- Langley, P. (2000). Crafting papers on machine learning. In Langley, P., editor, *Proceedings of the 17th International Conference on Machine Learning (ICML 2000)*, pages 1207–1216, Stanford, CA. Morgan Kaufmann.
- LeCun, Y., Bengio, Y., and Hinton, G. (2015). Deep learning. *Nature*, 521:436–444.
- Leng, X. and Müller, H.-G. (2006). Time ordering of gene co-expression. *Biostatistics*, 7:569–584.
- Liu, X. and Yang, M. C. K. (2009). Simultaneous curve registration and clustering for functional data. *Computational Statistics & Data Analysis*, 53(4):1361–1376.
- Lohit, S., Wang, Q., and Turaga, P. (2019). Temporal transformer networks: Joint learning of invariant and discriminative time warping. *Proceedings of the IEEE/CVF Conference on Computer Vision and Pattern Recognition*, pages 12426–12435.
- Lu, Y., Herbei, R., and Kurtek, S. (2017). Bayesian registration of functions with a gaussian process prior. *Journal of Computational and Graphical Statistics*, 26:894–904.
- Marron, J. S., Ramsay, J. O., Sangalli, L. M., and Srivastava, A. (2015). Functional data analysis of amplitude and phase variation. *Statistical Science*, 30(4):468–484.
- Matuk, J., Bharath, K., Chkrebti, O., and Kurtek, S. (2022). Bayesian framework for simultaneous registration and estimation of noisy, sparse and fragmented functional data. *Journal of American Statistical Association*, 117(540):1964–1980.
- Müller, H.-G. (2005). Functional modelling and classification of longitudinal data. *Scandinavian Journal of Statistics*, 32:223–240.
- Nagi, J., Ducatelle, F., Caro, G. A. D., Ciresan, D., Meier, U., Giusti, A., Nagi, F., Schmidhuber, J., and Gambardella, L. M. (2011). Maxpooling convolutional neural networks for vision-based hand gesture recognition. *IEEE International Conference on Signal and Image Processing Applications*, pages 342–347.
- Ramsay, J. and Silverman, B. (2002). *Applied Functional data analysis: Methods and Case Studies*. Springer, 1st edition.

- Ramsay, J. and Silverman, B. (2005). *Functional data analysis*. Springer, 2nd edition.
- Ramsay, J. O. and Li, X. (1998). Curve registration. *Journal of the Royal Statistical Society: Series B*, 60(2):351–363.
- Sokolova, M. and Lapalme, G. (2009). A systematic analysis of performance measures for classification tasks. *Information Processing & Management*, 45(4):427–437.
- Srivastava, A. and Klassen, E. P. (2016). *Functional and shape data analysis*. Springer.
- Srivastava, A., Wu, W., Kurtek, S., Klassen, E., and Marron, J. S. (2011). Registration of functional data using fisher-rao metric. *arXiv 1103.3817*.
- Stinchcombe, M. (1999). Neural network approximation of continuous functionals and continuous functions on compactifications. *Neural Networks*, 12(3):467–477.
- Süli, E. and Mayers, D. (2003). *An Introduction to Numerical Analysis*. Cambridge University Press, 1st edition.
- Tang, L., Zeng, P., Shi, J. Q., and Kim, W.-S. (2022). Model-based joint curve registration and classification. *Journal of Applied Statistics*.
- Tang, R. and Müller, H.-G. (2008). Pairwise curve synchronization for functional data. *Biometrika*, 95:875–889.
- Thind, B., Mutani, K. K. S., and Cao, J. (2020). Neural networks as functional classifiers. *arXiv:2010.04305*, pages 1–9.
- Tucker, J. D., Wu, W., and Srivastava, A. (2013). Generative models for functional data using phase and amplitude separation. *Computational Statistics & Data Analysis*, 61:50–66.
- Wahba, G. (1990). *Splines Models for Observational Data*. CBMS-NSF Regional Conference Series in Applied Mathematics, 1st edition.
- Wang, J.-L., Chiou, J.-M., and Müller, H.-G. (2016). Review of functional data analysis. *Annual Review of Statistics and Its application*, 3:257–295.
- Wang, K. and Gasser, T. (1997). Alignment of curves by dynamic time warping. *Annals of Statistics*, 25(3):1251–1276.
- Wang, S. and Cao, G. (2024). Multiclass classification for multidimensional functional data through deep neural networks. *Electronic Journal of Statistics*, 18:1248–1292.

- Wang, S., Cao, G., and Shang, Z. (2023). Deep neural network classifier for multidimensional functional data. *Scandinavian Journal of Statistics*, pages 1–20.
- Yann, L., Yoshua, B., and Geoffrey, H. (2015). Deep learning. *Nature*, 521(7553):436–444.
- Yao, J., Mueller, J., and Wang, J. L. (2021). Deep learning for functional data analysis with adaptive basis layers. *Proceedings of the 38th International Conference on Machine Learning*.
- Yarotsky, D. (2018). Universal approximations of invariant maps by neural networks.

A Derivation of the gradient of the objective function in DeepFRC

By the chain rule, the gradient of the objective function with respect to any $\theta \in \Theta$ is derived as follows:

$$\frac{\partial \mathcal{L}(\Theta)}{\partial \theta} = \begin{cases} 2 \sum_{j=1}^C \frac{\sum_{i \in \{y_i=j\}} (Q_i(\gamma_i))^T \cdot \frac{\partial Q_i(\gamma_i)}{\partial \gamma_i} \cdot \frac{\partial \gamma_i}{\partial \theta}}{N^{(j)}} - \frac{\alpha_2}{N} \sum_{i=1}^N \sum_{j=1}^C \frac{y_{ij}}{\psi_{ij}} \cdot \frac{\partial \psi_{ij}}{\partial \theta} + \alpha_3 \theta, & \theta \in \Theta_1, \\ -\frac{\alpha_2}{N} \sum_{i=1}^N \sum_{j=1}^C \frac{y_{ij}}{\psi_{ij}} \cdot \frac{\partial \psi_{ij}}{\partial \theta} + \alpha_3 \theta, & \theta \in \Theta_2. \end{cases} \quad (\text{A.1})$$

Here, the gradient of the warped SRVF with respect to the warping function γ_i is given by:

$$\frac{\partial Q_i(\gamma_i)}{\partial \gamma_i}[k] = \dot{q}_i(\gamma_i(t_{ik})) \sqrt{\dot{\gamma}(t_{ik})} + q_i(\gamma_i(t_{ik})) \frac{\ddot{\gamma}(t_{ik})}{2\sqrt{\dot{\gamma}(t_{ik})}}, \quad k = 1, \dots, n. \quad (\text{A.2})$$

When computing the gradient of $\mathcal{L}_1(\Theta_1)$ with respect to the warped SRVF ($Q_i(\gamma_i)$), the mean SRVF ($\bar{Q}^{(j)}$) is treated as constant, updated using the arithmetic mean of the warped SRVF from the previous iteration (Chen and Srivastava, 2021). For $\theta \in \Theta_1$, the gradient $\frac{\partial \gamma_i}{\partial \theta}$ can be expressed as the product of gradients from integration, fully connected layers, and the 1D-CNN module. Similarly, $\frac{\partial \psi_{ij}}{\partial \theta}$ is derived from the gradient of l_2 fully connected layers, interpolation, integration, and the 1D-CNN module (Yann et al., 2015). For $\theta \in \Theta_2$, $\frac{\partial \psi_{ij}}{\partial \theta}$ involves the gradient from fully connected layers in the prediction module (Yann et al., 2015).

B Model selection of DeepFRC

The model’s hyperparameters include network-related parameters $\{l_1, \mathbf{k}, \mathbf{s}, l_2, \mathbf{n}, K\}$, loss-related parameters $\{\alpha_{uv}, \alpha_2, \alpha_3\}$, and training-related parameters (such as epoch size E , batch size, and learning rate, denoted by vector $\boldsymbol{\eta}$). To select the structure-related hyperparameters $\{l_1, \mathbf{k}, \mathbf{s}, l_2, \mathbf{n}, K\}$, we follow the procedure proposed by Wang et al. (2023). First, the dataset $\{(\mathbf{x}_i, y_i)\}_{i=1}^N$ is split into two subsets with a 4:1 ratio. For each combination of hyperparameters, the model is trained by minimizing $\mathcal{L}_{\text{train}}$ (Eq. (10)) on the larger subset, and testing error $\mathcal{L}_{\text{test}}$ is computed on the smaller subset. The combination minimizing \mathcal{R} is selected. Similarly, grid search is used to select the loss-related hyperparameters $\{\alpha_{uv}, \alpha_2, \alpha_3\}$.

In our model, we set $l_1 = 4$, $\mathbf{k} = (16, 32, 64)$, and $\mathbf{s} = (3, 3, 3)$ for the 1D-CNN module, following the setup of SrvfRegNet (Chen and Srivastava, 2021). We apply max-pooling (Nagi et al., 2011) and 1D batch normalization (Ioffe and Szegedy, 2015) after each layer to downsample inputs and stabilize training, and use global averaging (Krizhevsky et al., 2012) followed by the final fully connected layer to further reduce features and noise. For the basis representation module, we set

$K = 100$ with a Fourier basis. Finally, in the prediction module, we set $l_2 = 2$ and $\mathbf{n} = (8, 4)$. This configuration works well across all the datasets in this paper.

C Proof of Theorem 3.1

For simplicity, we assume $\mathbf{t}_i = (\frac{0}{T}, \dots, \frac{T}{T})$, where $[0, T]$ is the observed time range, in the following proof. Consider the function $f(x) = \sqrt{x}$, which is continuous on $[0, 1]$. For any $\varepsilon > 0$, there exists $\delta_1 > 0$ such that for all $|x_1 - x_2| < \delta_1$, we have $|\sqrt{x_1} - \sqrt{x_2}| < \varepsilon$. Similarly, since q is continuous, for any $\varepsilon > 0$, there exists $\delta_2 > 0$ such that for all $|x_1 - x_2| < \delta_2$, we have $|q(x_1) - q(x_2)| < \varepsilon$.

Let \mathcal{G} be the domain of the neural network's output function, and Γ be the domain of the alignment functions γ . Denote $\Phi : \mathcal{G} \rightarrow \Gamma$ as the mapping from the neural network output to the alignment functions. Since both input and output of the network are discrete, we consider values only at discrete points. We define $g_i^{(k)} = g_i(\frac{k}{T})$ to maintain consistency between discrete vectors and continuous functions. The mapping is defined as:

$$\tau_i \mapsto \tilde{\gamma}_i \mapsto \gamma_i,$$

$$\tilde{\gamma}_i\left(\frac{k}{T}\right) = \frac{\sum_{s=0}^k \left(\tau_i^{(s)}\right)^2}{\sum_{s=0}^T \left(\tau_i^{(s)}\right)^2}, \quad \gamma_i\left(\frac{k}{T}\right) = \frac{\sum_{s=0}^k \tilde{\gamma}_i^{(s)}}{\sum_{s=0}^T \tilde{\gamma}_i^{(s)}}.$$

Let τ_i be such that $\Phi(\tau_i) = \gamma_i$. Since $\Phi(t\tau_i) = \Phi(\tau_i)$ for all $t \neq 0$, we can assume, without loss of generality, that $\|g_i\|_2 = 1$.

By the approximation property of convolutional neural networks (Yarotsky, 2018) and classical universal approximation results (Cybenko, 1989; Funahashi, 1989; Hornik, 1991; Stinchcombe, 1999), for any $\delta_4 > 0$, there exists a neural network NN_Θ with parameters Θ such that

$$\sup_i \|NN_\Theta(\mathbf{x}_i) - \tau_i\|_2 < \delta_4.$$

Let $\hat{\tau}_i = NN_\Theta(\mathbf{x}_i)$. We now aim to show that for sufficiently small $|\tau_i - \hat{\tau}_i|$, we also have $|\gamma_i - \hat{\gamma}_i|$ sufficiently small.

$$\begin{aligned}
\left| \tilde{\gamma}_i \left(\frac{k}{T} \right) - \hat{\gamma}_i \left(\frac{k}{T} \right) \right| &= \left| \frac{\sum_{s=0}^k \tau_i^2 \left(\frac{s}{T} \right)}{\sum_{s=0}^T \tau_i^2 \left(\frac{s}{T} \right)} - \frac{\sum_{s=0}^k \hat{\tau}_i^2 \left(\frac{s}{T} \right)}{\sum_{s=0}^T \hat{\tau}_i^2 \left(\frac{s}{T} \right)} \right| \\
&\leq \left| \frac{\sum_{s=0}^k \tau_i^2 \left(\frac{s}{T} \right)}{\sum_{s=0}^T \tau_i^2 \left(\frac{s}{T} \right)} - \frac{\sum_{s=0}^k \hat{\tau}_i^2 \left(\frac{s}{T} \right)}{\sum_{s=0}^T \tau_i^2 \left(\frac{s}{T} \right)} \right| + \left| \frac{\sum_{s=0}^k \hat{\tau}_i^2 \left(\frac{s}{T} \right)}{\sum_{s=0}^T \tau_i^2 \left(\frac{s}{T} \right)} - \frac{\sum_{s=0}^k \hat{\tau}_i^2 \left(\frac{s}{T} \right)}{\sum_{s=0}^T \hat{\tau}_i^2 \left(\frac{s}{T} \right)} \right| \\
&\leq \sum_{s=0}^k \left(\tau_i \left(\frac{s}{T} \right) + \hat{\tau}_i \left(\frac{s}{T} \right) \right) \delta_4 + (1 + \delta_4)^2 \frac{(2 + \delta_4) \delta_4}{(1 - \delta_4)^2} \\
&\leq \sum_{s=0}^k \left(\tau_i \left(\frac{s}{T} \right) + \hat{\tau}_i \left(\frac{s}{T} \right) \right) \delta_4 + 27 \delta_4 = M_k^{(1)} \delta_4.
\end{aligned}$$

Therefore, we have

$$\|\tilde{\gamma}_i - \hat{\gamma}_i\|_2 \leq \sqrt{\sum_{k=0}^T M_k^{(1)}} = M_{-1}^{(1)} \delta_4.$$

By Hölder's inequality $\|f\|_2 \leq \|f\|_1 \leq \sqrt{T+1} \|f\|_2$, we have

$$\|\tilde{\gamma}_i - \hat{\gamma}_i\|_1 \leq \sqrt{T+1} M_{-1}^{(1)} \delta_4.$$

Note that $\|\tilde{\gamma}_i\|_1 \geq \tilde{\gamma}_i \left(\frac{T}{T} \right) = 1$. On the other hand, for γ_i , we have

$$\begin{aligned}
\left| \gamma_i \left(\frac{k}{T} \right) - \hat{\gamma}_i \left(\frac{k}{T} \right) \right| &= \left| \frac{\sum_{s=0}^k \tilde{\gamma}_i \left(\frac{s}{T} \right)}{\sum_{z=0}^T \tilde{\gamma}_i \left(\frac{z}{T} \right)} - \frac{\sum_{s=0}^k \hat{\gamma}_i \left(\frac{s}{T} \right)}{\sum_{z=0}^T \hat{\gamma}_i \left(\frac{z}{T} \right)} \right| \\
&= \left| \frac{\sum_{s=0}^k \tilde{\gamma}_i \left(\frac{s}{T} \right)}{\sum_{z=0}^T \tilde{\gamma}_i \left(\frac{z}{T} \right)} - \frac{\sum_{s=0}^k \tilde{\gamma}_i \left(\frac{s}{T} \right)}{\sum_{z=0}^T \hat{\gamma}_i \left(\frac{z}{T} \right)} + \frac{\sum_{s=0}^k \tilde{\gamma}_i \left(\frac{s}{T} \right)}{\sum_{z=0}^T \hat{\gamma}_i \left(\frac{z}{T} \right)} - \frac{\sum_{s=0}^k \hat{\gamma}_i \left(\frac{s}{T} \right)}{\sum_{z=0}^T \tilde{\gamma}_i \left(\frac{z}{T} \right)} \right| \\
&\leq \left| \frac{\sum_{s=0}^k \tilde{\gamma}_i \left(\frac{s}{T} \right)}{\sum_{z=0}^T \tilde{\gamma}_i \left(\frac{z}{T} \right)} - \frac{\sum_{s=0}^k \hat{\gamma}_i \left(\frac{s}{T} \right)}{\sum_{z=0}^T \tilde{\gamma}_i \left(\frac{z}{T} \right)} \right| + \left| \frac{\sum_{s=0}^k \hat{\gamma}_i \left(\frac{s}{T} \right)}{\sum_{z=0}^T \tilde{\gamma}_i \left(\frac{z}{T} \right)} - \frac{\sum_{s=0}^k \hat{\gamma}_i \left(\frac{s}{T} \right)}{\sum_{z=0}^T \hat{\gamma}_i \left(\frac{z}{T} \right)} \right| \\
&\leq \left| \frac{\sum_{s=1}^k \left(\tilde{\gamma}_i \left(\frac{s}{T} \right) - \hat{\gamma}_i \left(\frac{s}{T} \right) \right)}{\sum_{z=0}^T \tilde{\gamma}_i \left(\frac{z}{T} \right)} \right| + \|\hat{\gamma}_i\|_1 \left| \frac{\sum_{s=0}^k \left(\hat{\gamma}_i \left(\frac{s}{T} \right) - \tilde{\gamma}_i \left(\frac{s}{T} \right) \right)}{\left(\sum_{z=0}^T \tilde{\gamma}_i \left(\frac{z}{T} \right) \right) \left(\sum_{z=0}^T \hat{\gamma}_i \left(\frac{z}{T} \right) \right)} \right| \\
&\leq \frac{k \sqrt{T+1} M_{-1}^{(1)} \delta_4}{\|\tilde{\gamma}_i\|_1} + \left(\|\tilde{\gamma}_i\|_1 + \sqrt{T+1} M_{-1}^{(1)} \delta_4 \right) \frac{\delta_4}{\|h_i\|_1 \left(\|\tilde{\gamma}_i\|_1 - \sqrt{T+1} M_{-1}^{(1)} \delta_4 \right)} \\
&\leq M_k^{(2)} \delta_4 \quad \text{for some } M_k^{(2)}.
\end{aligned}$$

Such that we have

$$\|\gamma_i - \hat{\gamma}_i\|_2 \leq \sqrt{\sum_{k=0}^T M_k^{(2)}} := M_{-1}^{(2)} \delta_4.$$

Recall that $Q_i(\gamma_i)\left(\frac{k}{T}\right) = (q_i \circ \gamma_i)\left(\frac{k}{T}\right) \cdot \sqrt{\dot{\gamma}_i\left(\frac{k}{T}\right)}$. Using the conditions that q_i and γ_i are bounded, we can bound the difference between $Q_i(\gamma_i)$ and $Q_i(\hat{\gamma}_i)$ by:

$$\begin{aligned} & \left| Q_i(\gamma_i)\left(\frac{k}{T}\right) - Q_i(\hat{\gamma}_i)\left(\frac{k}{T}\right) \right| \\ & \leq \left| q_i \circ \gamma_i\left(\frac{k}{T}\right) \cdot \left(\sqrt{\dot{\gamma}_i\left(\frac{k}{T}\right)} - \sqrt{\dot{\hat{\gamma}}_i\left(\frac{k}{T}\right)} \right) \right| + \left| \sqrt{\dot{\hat{\gamma}}_i\left(\frac{k}{T}\right)} \cdot \left(q_i \circ \gamma_i\left(\frac{k}{T}\right) - q_i \circ \hat{\gamma}_i\left(\frac{k}{T}\right) \right) \right| \\ & \leq \sup_t |q_i(t)| \cdot \left| \sqrt{\dot{\gamma}_i\left(\frac{k}{T}\right)} - \sqrt{\dot{\hat{\gamma}}_i\left(\frac{k}{T}\right)} \right| + \sup_t \sqrt{\dot{\gamma}_i(t)} \cdot \left| q_i\left(\gamma_i\left(\frac{k}{T}\right)\right) - q_i\left(\hat{\gamma}_i\left(\frac{k}{T}\right)\right) \right|. \end{aligned}$$

We use $\frac{\hat{\gamma}_i\left(\frac{k+1}{T}\right) - \hat{\gamma}_i\left(\frac{k-1}{T}\right)}{\frac{2}{T}}$ to approximate the derivative for $\hat{\gamma}_i$, so we have

$$\begin{aligned} \left| \dot{\gamma}_i\left(\frac{k}{T}\right) - \dot{\hat{\gamma}}_i\left(\frac{k}{T}\right) \right| & \leq \left| \dot{\gamma}_i\left(\frac{k}{T}\right) - \frac{\gamma_i\left(\frac{k+1}{T}\right) - \gamma_i\left(\frac{k-1}{T}\right)}{\frac{2}{T}} \right| + \left| \frac{\gamma_i\left(\frac{k+1}{T}\right) - \gamma_i\left(\frac{k-1}{T}\right)}{\frac{2}{T}} - \frac{\hat{\gamma}_i\left(\frac{k+1}{T}\right) - \hat{\gamma}_i\left(\frac{k-1}{T}\right)}{\frac{2}{T}} \right| \\ & \leq \left| \dot{\gamma}_i\left(\frac{k}{T}\right) - \frac{\gamma_i\left(\frac{k+1}{T}\right) - \gamma_i\left(\frac{k-1}{T}\right)}{\frac{2}{T}} \right| + T \sup_k \left| \gamma_i\left(\frac{k}{T}\right) - \hat{\gamma}_i\left(\frac{k}{T}\right) \right|. \end{aligned}$$

For $0 < \delta_3 < 1$, there exists a $T > 0$ such that:

$$\left| \dot{\gamma}_i\left(\frac{k}{T}\right) - \frac{\gamma_i\left(\frac{k+1}{T}\right) - \gamma_i\left(\frac{k-1}{T}\right)}{\frac{2}{T}} \right| < \delta_3, \quad \forall k.$$

Here we can choose $\delta_3 < \frac{\delta_1}{2}$, $\delta_2 = \min\{\delta_2, \frac{\delta_1}{2T}\}$, and $\delta_4 < \delta_2$. Then, we have

$$\left| \sqrt{\dot{\gamma}_i\left(\frac{k}{T}\right)} - \sqrt{\dot{\hat{\gamma}}_i\left(\frac{k}{T}\right)} \right| < \varepsilon, \quad \left| q_i \circ \gamma_i\left(\frac{k}{T}\right) - q_i \circ \hat{\gamma}_i\left(\frac{k}{T}\right) \right| < \varepsilon,$$

such that

$$\left| Q_i(\gamma_i)\left(\frac{k}{T}\right) - Q_i(\hat{\gamma}_i)\left(\frac{k}{T}\right) \right| \leq M_{-1}^{(3)}\varepsilon, \quad \text{where } M_{-1}^{(3)} \text{ is a constant.}$$

This means at each fixed point $\frac{k}{T}$, the difference between $Q_i(\gamma_i)$ and $Q_i(\hat{\gamma}_i)$ is bounded by $M_{-1}^{(3)}\varepsilon$, and it is straightforward to have

$$\|Q_i(\gamma_i) - Q_i(\hat{\gamma}_i)\|_2 \leq \sqrt{T}M_{-1}^3\varepsilon.$$

We finally get

$$\begin{aligned} \Delta Q_{\text{reg}}(\gamma^*, \hat{\gamma}) & = |Q_{\text{reg}}(\gamma^*) - Q_{\text{reg}}(\hat{\gamma})| \\ & = \left| \sum_{j=1}^C \frac{1}{N^{(j)}} \sum_{i \in \{y_i=j\}} \|Q_i(\gamma_i^*) - \bar{Q}^{(j)}\|^2 - \sum_{j=1}^C \frac{1}{N^{(j)}} \sum_{i \in \{y_i=j\}} \|Q_i(\hat{\gamma}_i) - \bar{Q}^{(j)}\|^2 \right| \\ & \leq \sum_{j=1}^C \frac{1}{N^{(j)}} \sum_{i \in \{y_i=j\}} \left| \|Q_i(\gamma_i^*) - \bar{Q}^{(j)}\|^2 - \|Q_i(\hat{\gamma}_i) - \bar{Q}^{(j)}\|^2 \right|. \end{aligned}$$

We now simplify $\frac{1}{N^{(j)}} \sum_{i \in \{y_i=j\}} \left| \|Q_i(\gamma_i^*) - \bar{Q}^{(j)}\|_2^2 - \|Q_i(\hat{\gamma}_i) - \bar{Q}^{(j)}\|_2^2 \right|$ as

$$\frac{1}{N^{(j)}} \sum_{i \in \{y_i=j\}} \left| \|a_i\|_2^2 + \|c\|_2^2 + 2\langle a_i, b_i \rangle + 2\langle b_i, c \rangle + 2\langle a_i, c \rangle \right|,$$

where $a_i = Q_i(\gamma_i) - Q_i(\hat{\gamma}_i)$, $b_i = Q_i(\hat{\gamma}_i) - \bar{Q}^{(j)}$, $c = \bar{Q}^{(j)} - \bar{Q}^{(j)}$.

By the Cauchy-Schwarz inequality: $\langle x, y \rangle \leq \|x\|_2 \|y\|_2$, we have $\|a_i\|_2 \leq \sqrt{T} M_{-1}^{(3)} \varepsilon$, and $\|c\|_2 = \left\| \frac{1}{N^{(j)}} \sum_{i \in \{y_i=j\}} a_i \right\|_2 \leq \sqrt{T} M_{-1}^{(3)} \varepsilon$. We also have $\|b_i\|_2 \leq M^{(4)}$ due to the boundness of q_i and γ_i .

Thus, we have

$$\left| \frac{1}{N^{(j)}} \sum_{i \in \{y_i=j\}} \|Q_i(\gamma_i) - \bar{Q}^{(j)}\|_2^2 - \frac{1}{N^{(j)}} \sum_{i \in \{y_i=j\}} \|Q_i(\hat{\gamma}_i) - \bar{Q}^{(j)}\|_2^2 \right| \leq 4T \left(M_{-1}^{(3)} \right)^2 \varepsilon^2 + 4\sqrt{T} M_{-1}^3 M^{(4)} \varepsilon.$$

Therefore, it is straightforward to have

$$\Delta Q_{\text{reg}}(\gamma^*, \hat{\gamma}) \leq 4CT \left(M_{-1}^{(3)} \right)^2 \varepsilon^2 + 4C\sqrt{T} M_{-1}^{(3)} M^{(4)} \varepsilon.$$

D Proof of Theorem 3.3

Based on Theorem 2 from Yao et al. (2021), we only need to verify that the loss function and its gradient are both Lipschitz continuous. Since the mean SRVF ($\bar{Q}^{(j)}$'s) are treated as constants when computing their gradients, and we have the condition that there exists $\epsilon_0 > 0$, such that $|\bar{Q}^{(u)} - \bar{Q}^{(v)}| \geq \epsilon_0$ for $1 \leq u < v \leq C$, we can omit the term $\sum_{1 \leq u < v \leq C} \alpha_{uv} \|\bar{Q}^{(u)} - \bar{Q}^{(v)}\|^{-1}$, and simplify the loss function of DeepFRC for any individual as

$$l(\hat{f}_{\Theta}(\mathbf{x}_i), y_i) = \sum_{j=1}^C \|Q_i - \bar{Q}^{(j)}\| \mathbb{1}_{\{i \in \{y_i=j\}\}} - \sum_{j=1}^C y_{ij} \log \psi_{ij}.$$

The loss function is obviously continuous for $\psi_{ij} \geq \epsilon_0$, as $\frac{1}{z}$ is continuous everywhere except at zero. Similar to Eqs. (A.1) and (A.2), the gradient of l with respect to any $\theta \in \Theta$ can be easily derived. These gradients can be expressed as products of gradients from ReLU, max pooling, etc., which are Lipschitz continuous. Therefore, the theorem follows directly from Theorem 3.8 in Hardt et al. (2016).

E Experimental Details

E.1 Description of Simulated Datasets

The parameter settings for the simulated datasets are shown in the following table. We split the balanced dataset into training, validation, and test sets with sizes 1600, 400, and 4000, respectively.

Table A1: Parameter setting for simulated data

Index	(01)	(02)	(11)	(12)
a_i	$13 + U(-0.5, 0.5)$	$12.5 + U(-1, 1)$	$12 + U(-1, 1)$	$13 + U(-1.5, 1.5)$
μ	0.250	0.715	0.225	0.695
σ_i	$0.06 + U(-0.003, 0.003)$	$0.075 + U(-0.003, 0.003)$	$0.06 + U(-0.003, 0.003)$	$0.1 + U(-0.003, 0.003)$

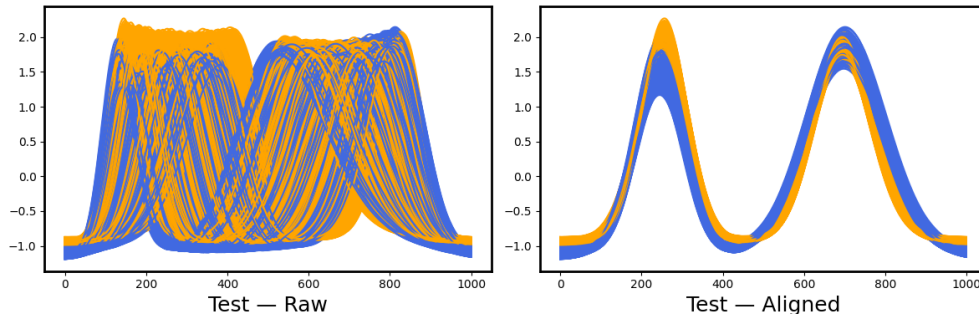


Figure A1: Visualization of alignment by DeepFRC on simulated test data

E.2 Description of Real Datasets

The Wave dataset (Liu and Yang, 2009) consists of eight simple gestures generated using accelerometers, collected through a particular procedure. For a participant, gestures are gathered when they hold a device and repeat certain gestures multiple times during a time period. The dataset includes X, Y, and Z dimensions with 8 classes. Here, we selected the X dimension and classes 2 and 8 for the experiment. There are 1120 samples with label partition 591/529, and the train/validation/test split is 320/80/720, with each sample having 315 time points.

The Yoga dataset consists of images of two actors (one male, one female) transitioning between yoga poses in front of a green screen. The task is to classify the images based on the actor’s gender. Each image was transformed into a one-dimensional series by measuring the distance from the outline of the actor to the center. The dataset contains 3300 samples with label partition 1770/1530, and the train/validation/test split is 800/200/2300. Each sample has 426 time points.

The Symbol dataset involves 13 participants, who were asked to replicate a randomly appearing symbol. There were 3 possible symbols, creating a total of 6 classes, and each participant made approximately 30 attempts. The dataset contains X-axis motion data recorded during the process of drawing the shapes. We conduct experiments on both the 2-class and 3-class cases using the Symbol dataset. In the 2-class case, there are 343 samples with label partition 182/167, and the train/validation/test split is 115/28/200. In the 3-class case, there are 510 samples with label partition 182/167/161, and the train/validation/test split is 168/42/300. Each sample has 398 time points.

E.3 Implementation Details of All Models on Real Data

For all datasets, the functional input is Z-score standardized entry-wise based on the mean function and standard deviation. To handle missing values (such as NAs) in the functional input, we use the `BasisSmoother` function from the `skfda.preprocessing.smoothing` module in Python to impute missing values.

The `DeepFRC` network is implemented as a PyTorch neural network. The hyperparameter settings for `DeepFRC` are shown in Table A2. In the discussion of stability with respect to basis

Table A2: Hyperparameter setting for `DeepFRC` on four real datasets

Case	α_{uv}	α_2	$lr_{\text{registration}}$	$lr_{\text{classification}}$
Wave	3000	50	1e-3	1e-3
Yoga	600	15	1e-3	5e-4
Symbol (2 classes)	300	15	1e-3	1e-3
Symbol (3 classes)	10	10	1e-3	1e-3

expansion for `DeepFRC`, we compute Fourier, B-spline, and Polynomial scores as follows: The Fourier scores are obtained using the fast Fourier transform function `rfft` from `torch.nn.fft`, extracting the first 100 scores. The B-spline scores are derived from the cubic B-spline basis with 98 knots uniformly distributed over the interval $[0, 1]$, resulting in exactly 100 B-spline basis functions. The Polynomial scores are obtained using the Chebyshev polynomial orthogonal basis, taking the first 100 Chebyshev polynomial functions. The B-spline and Polynomial scores are both calculated using the `BasisSmoother` function from the `skfda.preprocessing.smoothing` module in Python.

The model `SrvfRegNet` processes functional data through a learnable pre-warping block with three 1D convolutional layers (16, 32, 64 channels, kernel size 3, ReLU/BatchNorm/pooling), followed by a fully connected linear layer to generate warping functions. It applies time warping by minimizing the SRVF loss under an MSE criterion. The input data is the full functional data requiring alignment. The output of this network is the time-warping function that can generate aligned functional data. Both `FCNNraw` and `FCNNfourier` have the same architecture: a 3-layer MLP, with the input layer consisting of n observations or 100 Fourier scores (by default), followed by hidden layers with dimensions $[16, 8]$, and finally outputting the classification results. Each layer is equipped with Layer Normalization, the ReLU activation function, and a dropout rate of 0.1. The input of `FCNNraw` is the raw data, while the input of `FCNNfourier` is derived from the first 100 Fourier coefficients of the functional data. `SrvfRegNet` and `FCNNfourier` can be considered as two separate parts of `DeepFRC`. The models `FuncNN` and `ADAFNN` both take the entire curve as input. `FuncNN` uses a manually chosen basis expansion, while `ADAFNN` employs an adaptively learned basis layer

for representing curve data. We use the default architecture for the models `SrvfRegNet`, `FuncNN`, and `ADAFNN`. All of these baseline models are trained until the best performance is achieved.

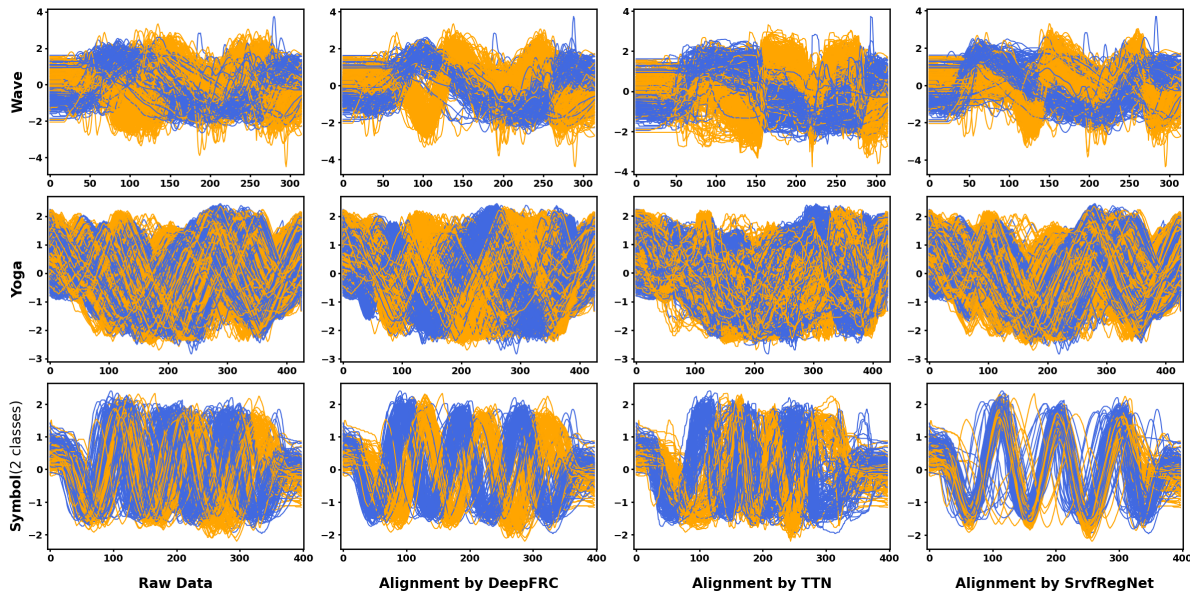


Figure A2: Comparison of alignment performance by DeepFRC, TTN and SrvfRegNet across three two-class real datasets

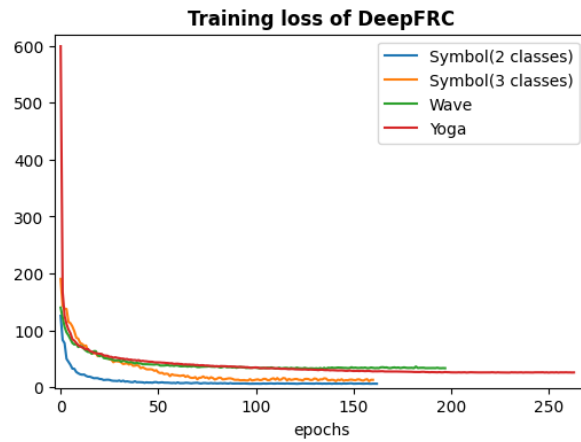


Figure A3: Training loss vs. epochs by DeepFRC across the four real-life datasets.